

Frequency Stability of Synchronous Machines and Grid-Forming Power Converters

Ali Tayyebi, Dominic Groß, *Member, IEEE*, Adolfo Anta, Friederich Kupzog and Florian Dörfler, *Member, IEEE*

Abstract—An inevitable consequence of the global power system transition towards nearly 100% renewable-based generation is the loss of conventional bulk generation by synchronous machines, their inertia, and accompanying frequency and voltage control mechanisms. This gradual transformation of the power system to a low-inertia system leads to critical challenges in maintaining system stability. Novel control techniques for converters, so-called grid-forming strategies, are expected to address these challenges and replicate functionalities that so far have been provided by synchronous machines. This article presents a low-inertia case study that includes synchronous machines and converters controlled under various grid-forming techniques. In this work 1) the positive impact of the grid-forming converters on the frequency stability of synchronous machines is highlighted, 2) a qualitative analysis which provides insights into the frequency stability of the system is presented, 3) we explore the behavior of the grid-forming controls when imposing the converter dc and ac current limitations, 4) the importance of the dc dynamics in grid-forming control design as well as the critical need for an effective ac current limitation scheme are reported, and lastly 5) we analyze how and when the interaction between the fast grid-forming converter and the slow synchronous machine dynamics can contribute to the system instability.

I. INTRODUCTION

At the heart of the energy transition is the change in generation technology; from fossil fuel based generation to converter interfaced renewable generation [1]. One of the major consequences of this transition towards a nearly 100% renewable system is the gradual loss of synchronous machines (SMs), their inertia, and control mechanisms. This loss of the rotational inertia changes the nature of the power system to a low-inertia network resulting in critical stability challenges [1]–[3]. On the other hand, low-inertia power systems are characterized by large-scale integration of generation interfaced by power converters, allowing frequency and voltage regulation at much faster time-scales compared to SMs [1], [4].

Indeed, power converters are already starting to provide new ancillary services, modifying their active and reactive

power output based on local measurements of frequency and voltage. However, because of the dependency on frequency measurements these *grid-following* control techniques only replicate the instantaneous inertial response of SMs after a contingency with a delay and result in degraded performance on the time scales of interest [5]. To resolve this issue, *grid-forming converters* (GFCs) are envisioned to be the cornerstone of future power systems. Based on the properties and functions of SMs, it is expected that grid-forming converters must support load-sharing/drooping, black-start, inertial response, and hierarchical frequency/voltage regulation. While these services might not be necessary in a future converter-based grid, a long transition phase is expected, where SMs and GFCs must be able to interact and ensure system stability.

Several grid-forming control strategies have been proposed in recent years [4]. *Droop control* mimics the speed droop mechanism present in SMs and is a widely accepted baseline solution [6]. As a natural further step, the emulation of SM dynamics and control led to so-called *virtual synchronous machine* (VSM) strategies [7]–[9]. Recently, *matching* control strategies that exploit structural similarities of converters and synchronous machine and *match* their dynamic behavior have been proposed [10]–[13]. In contrast, virtual oscillator control (VOC) uses GFCs to mimic the synchronizing behavior of Liénard-type oscillators and can globally synchronize a converter-based power system [14]. However, the nominal power injection of VOC cannot be specified. This limitation is overcome by *dispatchable virtual oscillator control* (dVOC) [15]–[17] that ensures synchronization to a pre-specified operating point that satisfies the ac power flow equations.

In this article, the dynamics of the converter dc-link capacitor, the response time of the dc power source, and its current limits is explicitly considered. We review four different grid-forming control strategies and combine them with standard low-level cascaded control design accounting for the ac voltage control and the ac current limitation and control [18]. We explore the various performance aspects of GFC control techniques in an electromagnetic transients (EMT) simulation of the IEEE 9-bus test system, namely: 1) the impact of GFCs on the frequency performance metrics e.g., nadir and rate of change of frequency (RoCoF) [19]–[22], 2) the response of GFCs under large load disturbances, 3) their behavior when imposing dc and ac current limitations, and 4) their response to the loss of SM and performance in a pure converter-based system. Furthermore, we provide an insightful qualitative analysis of the simulation results. The models used in this work are available online [23].

This study highlights the positive impact of GFCs on im-

This work was partially funded by the independent research fund of the the power system digitalization group at the Electric Energy Systems (EES) competence unit of the Austrian Institute for Technology (AIT), ETH Zürich funds, and by the European Unions Horizon 2020 research and innovation programme under grant agreement No. 691800. This article reflects only the authors views and the European Commission is not responsible for any use that may be made of the information it contains. A. Tayyebi (the corresponding author) is with AIT, 1210 Vienna, Austria, and also with the Automatic Control Laboratory, ETH Zürich, Switzerland. D. Groß is with the Department of Electrical and Computer Engineering, University of Wisconsin-Madison, Madison, WI 53706, USA. A. Anta and F. Kupzog are with AIT, and F. Dörfler is with the Automatic Control Laboratory, ETH Zürich, 8092 Zürich, Switzerland; E-mail: {ali.tayyebi-khameneh,adolfo.anta,friederich.kupzog}@ait.ac.at, dominic.gross@wisc.edu, and dorfler@ethz.ch.

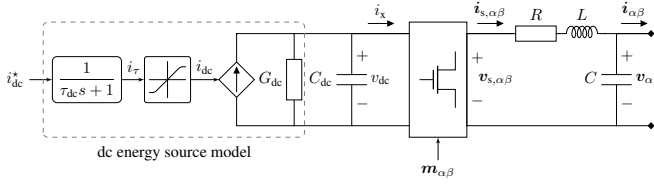


Fig. 1: Converter model in $\alpha\beta$ -coordinates with detailed dc energy source model based on (1)-(3).

proving the standard power system frequency stability metrics. Moreover, we observe that limiting the GFCs dc or ac current accompanied by the interaction of fast converters and slow synchronous machine dynamics can destabilize some grid-forming controls. This observation, highlights the importance of the dc dynamics in grid-forming control design as well as the critical need for an ac current limiting mechanism. Furthermore, we reveal a potentially destabilizing interaction between the fast synchronization of GFCs and the slow response of SMs (see [16], [24] for a similar observation on the interaction of GFCs and line dynamics). Lastly, this study shows that an all-GFCs (i.e., no-inertia) system can exhibit more resilience than a mixed SM-GFCs (i.e., low-inertia) system with respect to the large load variations.

The remainder of this article is structured as follows: Section II reviews the modeling approach. Section III presents the system dynamics and adopted grid-forming control techniques. The simulation-based analysis of the study is discussed in Section IV. Section V presents a qualitative analysis of the observations made in case studies. The concluding statements and agenda of future work are reported in Section VI. And the choice of control parameters is described in Appendix A.

II. MODEL DESCRIPTION

Throughout this study, we use a test system comprised of power converters and synchronous machines. This section describes the models of the individual devices and components [23].

A. Converter Model

To begin with, we consider the converter model illustrated in Figure 1 in $\alpha\beta$ -coordinates [13], [25]

$$C_{dc}\dot{v}_{dc} = i_{dc} - G_{dc}v_{dc} - i_x, \quad (1a)$$

$$L\dot{i}_{s,\alpha\beta} = v_{s,\alpha\beta} - Ri_{s,\alpha\beta} - v_{\alpha\beta}, \quad (1b)$$

$$C\dot{v}_{\alpha\beta} = i_{s,\alpha\beta} - i_{\alpha\beta}, \quad (1c)$$

where C_{dc} denotes the dc-link capacitance, G_{dc} models dc losses, and, L , C , and R respectively denote the filter inductance, capacitance, and resistance. Moreover, v_{dc} represents the dc voltage, i_{dc} is the current flowing out of the controllable dc current source, $m_{\alpha\beta}$ denotes the modulation signal of the full-bridge averaged switching stage model, $i_x := (1/2)m_{\alpha\beta}^T i_{s,\alpha\beta}$ denotes the net dc current delivered to the switching stage, and $i_{s,\alpha\beta}$ and $v_{s,\alpha\beta} := (1/2)m_{\alpha\beta} v_{dc}$ respectively are the ac switching node current and voltage (i.e., before the output filter), $i_{\alpha\beta}$ and $v_{\alpha\beta}$ are the output current and voltage.

To obtain a realistic model of the dc energy source, we model its response time by a first order system

$$\tau_{dc}\dot{i}_{dc} = i_{dc}^* - i_{dc}, \quad (2)$$

where i_{dc}^* is the dc current reference, τ_{dc} is the dc source time constant, and i_{dc} denotes the current provided by the dc source. Moreover, the dc source current limitation is modeled by the saturation function

$$i_{dc} = \text{sat}(i_{dc}, i_{dc}^{\max}) = \begin{cases} i_{dc}^* & \text{if } |i_{dc}^*| < |i_{dc}^{\max}|, \\ \text{sgn}(i_{dc}^*) i_{dc}^{\max} & \text{if } |i_{dc}^*| \geq |i_{dc}^{\max}|, \end{cases} \quad (3)$$

where i_{dc}^{\max} is the maximum dc source current. Note that we implicitly assume that some storage element is present so that the dc source can support bidirectional power flow. In practice, the limit imposed by (3) corresponds to current limits of a dc-dc converter, current limits of an energy storage system, or PV / wind power generation limits. The impact of the dc source limitation (3) is investigated in Section IV. It is noteworthy that the converter must also limit its ac current to protect its semiconductor switches [26]. This ac current limitation is typically imposed via converter control design (see Section III for details).

B. Synchronous Machine Model

In this work we adopt an 8th order (i.e., including six electrical and two mechanical states), balanced, symmetrical, three-phase SM with a field winding and three damper windings on the rotor [2, Fig. 3.1]

$$\dot{\theta} = \omega, \quad (4a)$$

$$J\dot{\omega} = T_m - T_e - T_f, \quad (4b)$$

$$\dot{\psi}_{s,dq} = v_{s,dq} - r_s i_{s,dq} - \mathcal{J}_2 \psi_{s,dq}, \quad (4c)$$

$$\dot{\psi}_{f,d} = v_{f,d} - r_{f,d} i_{f,d}, \quad (4d)$$

$$\dot{\psi}_D = v_D - \mathcal{R}_D i_D, \quad (4e)$$

where θ denotes the rotor angle, J is the inertia constant, ω is the rotor speed, T_m , T_e and T_f denote the mechanical torque, electrical torque, and the friction winding torque (see [2, Sec. 5.7]). Moreover, $\psi_{s,dq} = [\psi_{s,d} \ \psi_{s,q}]^T$, $v_{s,dq} = [v_{s,d} \ v_{s,q}]^T$, and $i_{s,dq} = [i_{s,d} \ i_{s,q}]^T$ denote the stator winding flux, voltage, and current in dq-coordinates (with angle θ as in (4a)), $\mathcal{J}_2 = \begin{bmatrix} 0 & -1 \\ 1 & 0 \end{bmatrix}$ denotes the 90° rotation matrix, $\psi_{f,d}$, $v_{f,d}$, and $i_{f,d}$ denote the d-axis field winding flux, voltage and current. Furthermore, r_s and $r_{f,d}$ denote the stator and field winding resistances, $\psi_D = [\psi_{1d} \ \psi_{1q} \ \psi_{2q}]^T$, $v_D = [v_{1d} \ v_{1q} \ v_{2q}]^T$ and $i_D = [i_{1d} \ i_{1q} \ i_{2q}]^T$ are the linkage flux, voltage and current associated with three damper windings and $\mathcal{R}_D = \text{diag}(r_{1d}, r_{1q}, r_{2q})$ denotes the diagonal matrix of the damper winding resistances. Note that the windage friction (i.e., modeling friction between the rotor and air) term is commonly expressed as a speed dependent term e.g., $T_f = D_f \omega$ [2, Sec. 5.7] it is typically negligible for system-level studies and is included here for the sake of completeness and to highlight structural similarities of the SM and two-level voltage source converter with the control presented in Section III-E. Furthermore, the damping torque associated with the damper windings is included in the SM model (4) via the damper winding dynamics (4e). For more

details on the SM modeling and parameters computation the reader is referred to [2, Sec. 3.3], [3, Chap. 4].

We augment the system (4) with a ST1A type excitation dynamics with built-in automatic voltage regulator (AVR) [27, Fig. 21]. To counteract the well-known destabilizing effect of the AVR on the synchronizing torque, we equip the system with a simplified power system stabilizer comprised of a two-stage lead-lag compensator [3, Sec. 12.5]. Lastly, the governor and turbine dynamics are respectively modeled by proportional speed droop control and first order turbine dynamics

$$p = p^* + d_p (\omega^* - \omega), \quad (5a)$$

$$\tau_g \dot{p}_\tau = p - p_\tau, \quad (5b)$$

where p^* denotes the power set-point, p is the governor output, d_p denotes the governor speed droop gain, and ω^* and ω denote nominal and measured frequency, respectively. Furthermore, τ_g denotes the turbine time constant and p_τ denotes the turbine output power. We refer the reader to [24, Fig. 2] for an illustration of the interplay between the SM model, the excitation dynamics, the PSS and governor dynamics. Lastly, the Matlab/Simulink implementation of the SM model can be found in [23].

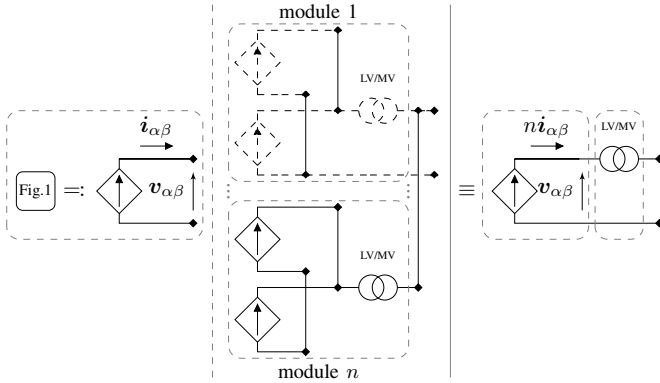


Fig. 2: Equivalent model of an individual converter module (left), large-scale multi-converter system consisting of n identical modules (middle), and aggregate model (right).

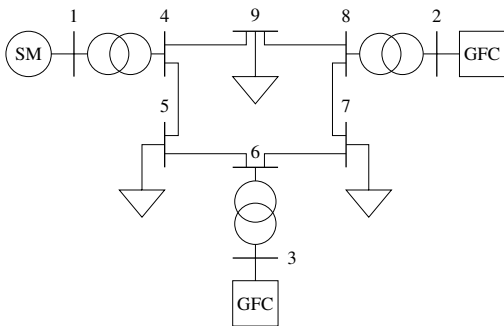


Fig. 3: IEEE 9-bus test system with a synchronous machine, two large-scale multi-converter systems (i.e., aggregate GFCs), and constant impedance loads.

C. Network Model

To study the transmission level dynamics of a low-inertia power system, we use Sim Power Systems to perform an EMT simulation of the IEEE 9-bus test system shown in Figure 3 [4], [28]. We model the lines via nominal π sections (i.e., with RLC dynamics), model the transformers via three-phase linear transformer models, and consider constant impedance loads (see Table I for the parameters). We emphasize that the line dynamics cannot be neglected in the presence of grid-forming converters due to potential adverse interactions between their fast response and the line dynamics [16], [24], [29].

Remark 1. (Aggregate Converter Model)

In this case study, each GFC in Figure 3 is an aggregate model of 200 commercial converter modules (see Table I for the parameters). Each module is rated at 500 kVA and the aggregate model is rated at 100 MVA, which is equal to the SM rating. Each module is interfaced to a medium voltage line via a LV-MV transformer (see Figure 2). We derive the parameters of the aggregate transformer model by assuming a parallel connection of 100 commercial transformers rated at 1.6 MVA (see Table I). A detailed presentation and derivation of the model aggregation is out of the scope of this work, but we follow developments analogous to [30]–[32] in deriving the equivalent aggregate converter parameters.

III. GRID-FORMING CONTROL ARCHITECTURES

Grid-forming control strategies control (see Figure 4) a converter through the reference current i_{dc}^* for the dc energy source (1a) and the modulation signal $m_{\alpha\beta}$ for the dc-ac conversion stage (1) (see Figure 1). In the following, we briefly review the low-level cascaded control design (i.e., ac voltage control, current limitation and control) for two-level voltage source converters that tracks a voltage reference provided by a reference model (i.e., grid-forming control). Moreover, we propose a controller for the converter dc voltage which defines the reference dc current. Because their design is independent of the choice of the reference model, we first discuss the cascaded voltage / current control and the dc-side control. Subsequently, we review four common grid-forming control strategies. For each strategy, we describe the angle dynamics, frequency dynamics and ac voltage magnitude regulation. Throughout this section we will employ the three phase abc, $\alpha\beta$ and dq-coordinates (see [25, Sec. 4.5 and 4.6] for details on the transformations). We remind the reader that the Simulink implementation of the controls presented in the forthcoming subsections is available online [23].

A. Low-Level Cascaded Control Design

1) *AC Voltage Control*: we employ a standard converter control architecture that consists of a reference model providing a reference voltage \hat{v}_{dq} with angle $\angle \hat{v}_{dq} = \theta$ and magnitude $\|\hat{v}_{dq}\|$. The modulation signal $m_{\alpha\beta}$ is determined by cascaded proportional-integral (PI) controllers that are implemented in dq-coordinates (rotating with the reference angle θ) and track the voltage reference \hat{v}_{dq} (see [18]). The voltage

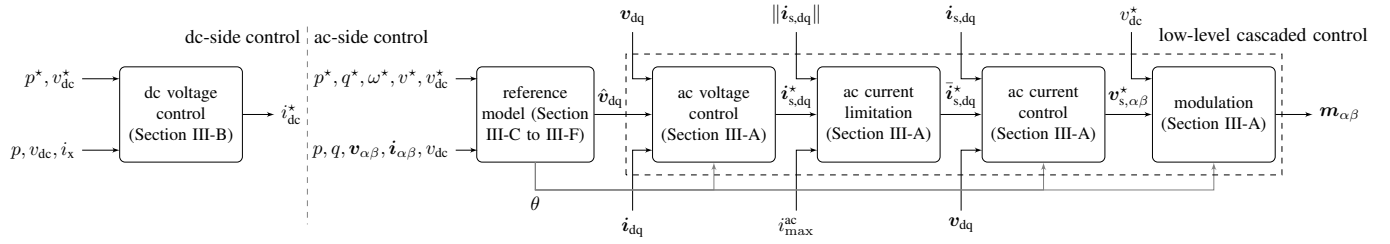


Fig. 4: Grid-forming control architecture with reference models described in subsections III-C to III-F.

tracking error $\hat{v}_{dq} - v_{dq}$ is used to compute the reference $\mathbf{i}_{s,dq}^* = [i_{sd}^* \ i_{sq}^*]^T$ for the switching node current $\mathbf{i}_{s,dq}$

$$\dot{\mathbf{x}}_{v,dq} = \hat{v}_{dq} - v_{dq}, \quad (6a)$$

$$\mathbf{i}_{s,dq}^* := \underbrace{\mathbf{i}_{dq} + C\omega \mathcal{J}_2 v_{dq}}_{\text{feed-forward terms}} + \underbrace{\mathcal{K}_{v,p} (\hat{v}_{dq} - v_{dq}) + \mathcal{K}_{v,i} \mathbf{x}_{v,dq}}_{\text{PI control}} \quad (6b)$$

here $\mathbf{x}_{v,dq} = [x_{v,d} \ x_{v,q}]^T$ denotes the integrator state, $\mathbf{v}_{dq} = [v_d \ v_q]^T$ denotes the output voltage measurement, $\hat{v}_{dq} = [\hat{v}_d \ 0]^T$ denotes the reference voltage, $\mathbf{i}_{dq} = [i_d \ i_q]^T$ denotes the output current, \mathcal{I}_2 is the 2-D identity matrix, $\mathcal{K}_{v,p} = k_{v,p} \mathcal{I}_2$ and $\mathcal{K}_{v,i} = k_{v,i} \mathcal{I}_2$ denote diagonal matrices of proportional and integral gains, respectively.

2) *AC Current Limitation*: We assume that the underlying current controller or low-level protections of the converter limit the ac current. We model this in abstraction by scaling down the reference current $\|\mathbf{i}_{s,dq}^*\|$ if it exceeds the pre-defined converter current limit $i_{s,dq}^{ac,max}$ [33, Sec. III], i.e.,

$$\bar{\mathbf{i}}_{s,dq}^* := \begin{cases} \mathbf{i}_{s,dq}^* & \text{if } \|\mathbf{i}_{s,dq}^*\| \leq i_{s,dq}^{ac,max}, \\ \gamma_i \mathbf{i}_{s,dq}^* & \text{if } \|\mathbf{i}_{s,dq}^*\| > i_{s,dq}^{ac,max}, \end{cases} \quad (7)$$

where $\bar{\mathbf{i}}_{s,dq}^*$ denotes the limited reference current that preserves the direction of $\mathbf{i}_{s,dq}^*$ and $\gamma_i := (i_{s,dq}^{ac,max} / \|\mathbf{i}_{s,dq}^*\|)$. We emphasize that limiting the ac current can have a strong impact on the stability margins and dynamics of grid-forming power converters [34]. While numerous different strategies have been proposed to limit the ac current injection of voltage source converters with grid-forming controls [26], [33], [35]–[39] the problem of designing a robust ac current limitation strategy that effectively reacts to the load-induced over-current and grid faults is an open research problem. Moreover, complex current limitation strategies typically require careful tuning of the controllers. Therefore, to provide a clear and concise investigation of the behavior of the existing grid-forming control solutions, we use the simple ac current limiting strategy (7).

3) *AC Current Control*: in order to implement this scheme, a PI controller for the current $\mathbf{i}_{s,dq} = [i_{s,d} \ i_{s,q}]^T$ is used to track $\bar{\mathbf{i}}_{s,dq}^*$

$$\dot{\mathbf{x}}_{i,dq} = \bar{\mathbf{i}}_{s,dq}^* - \mathbf{i}_{s,dq}, \quad (8a)$$

$$\mathbf{v}_{s,dq}^* := \underbrace{\mathbf{v}_{dq} + \mathcal{Z} \mathbf{i}_{s,dq}}_{\text{feed-forward terms}} + \underbrace{\mathcal{K}_{i,p} (\bar{\mathbf{i}}_{s,dq}^* - \mathbf{i}_{s,dq}) + \mathcal{K}_{i,i} \mathbf{x}_{i,dq}}_{\text{PI control}}, \quad (8b)$$

where $\mathcal{Z} = L\omega \mathcal{J}_2 + R\mathcal{I}_2$, $\mathbf{v}_{s,dq}^* = [v_{s,d}^* \ v_{s,q}^*]^T$ is the reference for the switching node voltage (i.e., before output filter in Figure 1), $\mathbf{x}_{i,dq} = [x_{i,d} \ x_{i,q}]^T$ denotes the integrator state, and

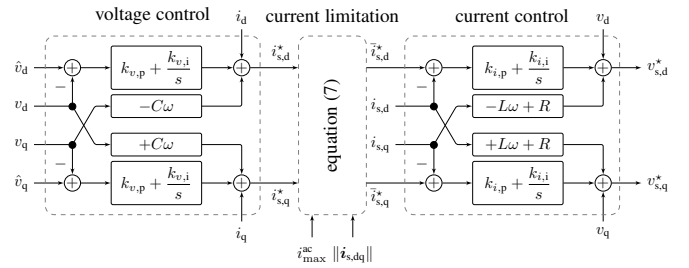


Fig. 5: Block diagram of the low-level cascaded control design (6)-(8) in dq-coordinates rotating with the angle θ provided by the reference model.

$\mathcal{K}_{i,p} = k_{i,p} \mathcal{I}_2$ and $\mathcal{K}_{i,i} = k_{i,i} \mathcal{I}_2$ denote the diagonal matrices of proportional and integral gains, respectively. Note that the first two terms of the right hand side of (6b) and (8b) are feed-forward terms. Finally, the modulation signal $\mathbf{m}_{\alpha\beta}$ is given by

$$\mathbf{m}_{\alpha\beta} = \frac{2\mathbf{v}_{s,\alpha\beta}^*}{v_{dc}^*}, \quad (9)$$

where $\mathbf{v}_{s,\alpha\beta}^*$ is the $\alpha\beta$ -coordinates image of $\mathbf{v}_{s,dq}^*$ defined in (8) and v_{dc}^* denotes the nominal converter dc voltage.

B. DC Voltage Control

The dc current reference i_{dc}^* that is tracked by the controllable dc source (2) is given by a proportional control for the dc voltage and feed-forward terms based on the nominal ac active power injection p^* and the filter losses

$$i_{dc}^* = \underbrace{k_{dc} (v_{dc}^* - v_{dc})}_{\text{proportional control}} + \underbrace{\frac{p^*}{v_{dc}^*} + \left(G_{dc} v_{dc} + \frac{v_{dc} i_{x} - p}{v_{dc}^*} \right)}_{\text{power injection and loss feed-forward}}, \quad (10)$$

where $v_{dc} i_x$ is the dc power flowing into the switches, p is the ac power injected into the grid, and the last term on the right hand side of (10) implements a feed-forward power control that compensates the filter losses. The loss compensation is required to ensure exact tracking of the power reference by matching control (see Section III-E) and also improves the dc voltage regulation for the other control strategies considered in this study. Thus, to employ an identical dc voltage control, we apply (10) for all control strategies discussed throughout this work.

C. Droop Control

Droop control resembles the speed droop property (5a) of the SM governor [6] and trades off deviations of the power

injection (from its nominal value p^*) and frequency deviations (from ω^*)

$$\dot{\theta} = \omega, \quad (11a)$$

$$\omega = \omega^* + d_\omega (p^* - p), \quad (11b)$$

where d_ω denotes the droop gain. To replicate the service provided by the automatic voltage regulator (AVR) of synchronous machines we use a PI controller acting on the output voltage error

$$\hat{v}_d = k_p (v^* - \|v_{dq}\|) + k_i \int_0^t (v^* - \|v_{dq}(\tau)\|) d\tau. \quad (12)$$

to obtain the direct axis reference \hat{v}_d for the underlying voltage loop (v^* and $\|v_{dq}\|$ are the reference and measured voltage magnitude). We remark that $\hat{v}_q = 0$ and the reactive power injection varies such that exact voltage regulation is achieved.

D. Virtual Synchronous Machine

Many variations of virtual synchronous machines (VSMs) have been proposed [7], [8]. In this work, we consider the frequency dynamics induced by the synchronverter [8]

$$\dot{\theta} = \omega, \quad (13a)$$

$$J_r \dot{\omega} = \frac{1}{\omega^*} (p^* - p) + D_p (\omega^* - \omega), \quad (13b)$$

where $D_p (\omega^* - \omega)$ is commonly referred to as (virtual) damping [8, Sec. II-b] and is inspired by the speed droop response of a synchronous machine. Note that the speed dependent term in (13b) has no exact analogue in a synchronous machine. The response of SM damper windings and its turbine governor are on different time scales and the SM damper windings do not act relative to the nominal frequency. In contrast, the speed dependent term in (13b) provides both instantaneous damping and at steady-state (i.e., the equivalent to SM turbine governor droop) relative to the nominal frequency. Moreover, J_r is the virtual rotor's inertia constant. Note that the dynamics (13) reduce to droop control (11) when using $J_r/D_p \approx 0$ as

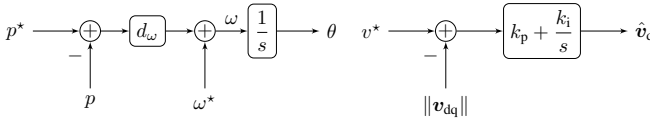


Fig. 6: Droop control frequency and ac voltage control block diagrams based on (11) and (12).

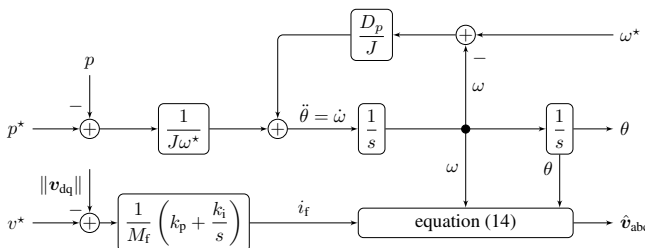


Fig. 7: Block diagram of a grid-forming VSM based (13)-(15).

recommended in [8]. These angle dynamics capture the main salient features of virtual synchronous machines, but do not suffer from drawbacks of more complicated implementations (see [4] for a discussion). The three-phase voltage induced by the VSM is given by

$$\hat{v}_{abc} = 2\omega M_f i_f \begin{bmatrix} \sin(\theta) & \sin(\theta - \frac{2\pi}{3}) & \sin(\theta - \frac{4\pi}{3}) \end{bmatrix}^T, \quad (14)$$

where M_f and i_f are respectively the virtual mutual inductance magnitude and excitation current. Similar to (12), we utilize input i_f to achieve exact ac voltage regulation via PI control and thereby replicate the function of the AVR of a synchronous machine

$$i_f = \frac{k_p}{M_f} (v^* - \|v_{dq}\|) + \frac{k_i}{M_f} \int_0^t (v^* - \|v_{dq}(\tau)\|) d\tau. \quad (15)$$

Transforming \hat{v}_{abc} to dq-coordinates with θ and ω as in (13), the voltage and current loops and modulation signal generation remain the same as (6)–(9).

E. Matching Control

Matching control is a grid-forming control strategy that exploits structural similarities between power converters and SMs [10]–[13], [40] and is based on the observation that the dc-link voltage - similar to the synchronous machine frequency - indicates power imbalances. Hence, the dc voltage, up to a constant factor, is used to drive the converter frequency. This control technique structurally matches the differential equations of a converter to those of a SM. Furthermore, analogous to the machine input torque, the dc current is used to control the ac power. The angle dynamics of matching control are represented by

$$\dot{\theta} = k_\theta v_{dc}, \quad (16)$$

where $k_\theta := \omega^*/v_{dc}^*$. Finally, the ac voltage magnitude is controlled through the modulation magnitude μ by a PI controller

$$\mu = k_p (v^* - \|v_{dq}\|) + k_i \int_0^t (v^* - \|v_{dq}(\tau)\|) d\tau. \quad (17)$$

The reference voltage for the voltage controller in $\alpha\beta$ -coordinates is given by:

$$\hat{v}_{\alpha\beta} = \mu [-\sin\theta \cos\theta]^T. \quad (18)$$

Transforming $\hat{v}_{\alpha\beta}$ to dq-coordinates with θ and ω as in (16), the voltage and current loops and modulation signal generation remain the same as (6)–(9).

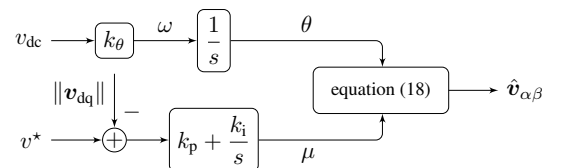


Fig. 8: Matching control block diagram based on (16)-(18).

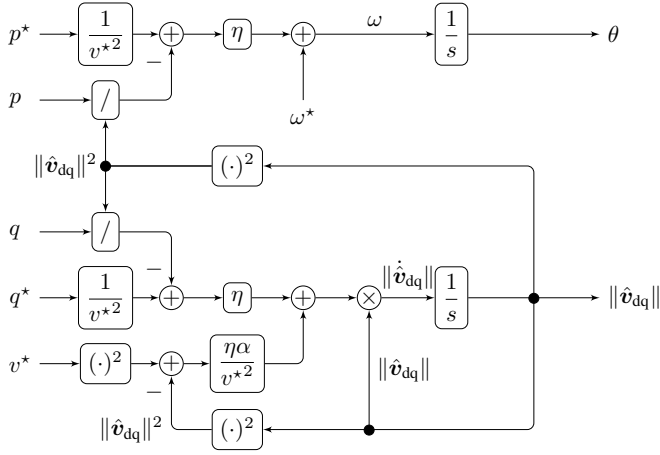


Fig. 9: Block diagram of dVOC in polar coordinates corresponding to (22). Note that singularity at $\|\hat{v}_{dq}\| = 0$ only appears in the dVOC implementation in polar coordinates but not in the implementation in rectangular coordinates, i.e., (21).

To further explain the matching concept, we replace v_{dc} in (1a) by ω/k_θ from (16) resulting in

$$\dot{\theta} = \omega, \quad (19a)$$

$$C_{dc}\dot{\omega} = k_\theta i_{dc} - k_\theta i_x - G_{dc}\omega. \quad (19b)$$

Recalling the SM's angle and frequency dynamics (4a)-(4b) and replacing T_f by $D_f\omega$

$$\dot{\theta} = \omega, \quad (20a)$$

$$J\dot{\omega} = T_m - T_e - D_f\omega, \quad (20b)$$

Comparing (19) and (20) reveals the structural matching of GFC dynamics to that of SM. Dividing (19b) by k_θ^2 to obtain the same units as in (20b) and matching variables results in $J_r = C_{dc}/k_\theta^2$, $D_f = G_{dc}/k_\theta^2$, $T_m = i_{dc}/k_\theta$, and $T_e = i_x/k_\theta$. In other words, using matching control the inertia constant of the GFC is linked to its internal energy storage, the dc-side losses $G_{dc}\omega$ are linked to the machine windage friction losses $D_f\omega$, and the frequency droop response is provided through the proportional dc voltage control $k_{dc}(v_{dc}^* - v_{dc}) = (k_{dc}/k_\theta)(\omega^* - \omega)$ (cf. (10)). The structural matching induced by (16) also extends to the converter ac filter and generator stator dynamics (see [11], [13] for a detailed derivation).

F. Dispatchable Virtual Oscillator Control

Dispatchable virtual oscillator control (dVOC) [15]–[17] is a decentralized grid-forming control strategy that guarantees almost global asymptotic stability for interconnected GFCs with respect to nominal voltage and power set-points [15], [16]. The analytic stability conditions for dVOC explicitly quantify the achievable performance and include the dynamics and transfer capacity of the transmission network [16].

The dynamics of dVOC in $\alpha\beta$ -coordinates are represented by

$$\dot{\hat{v}}_{\alpha\beta} = \omega^* \mathcal{J}_2 \hat{v}_{\alpha\beta} + \eta (\mathcal{K} \hat{v}_{\alpha\beta} - \mathcal{R}_2(\kappa) \hat{i}_{\alpha\beta} + \phi(v^*, \hat{v}_{\alpha\beta})), \quad (21)$$

where $\phi(v^*, \hat{v}_{\alpha\beta}) = (\alpha/v^{*2}) (v^{*2} - \|\hat{v}_{\alpha\beta}\|^2) \hat{v}_{\alpha\beta}$, $\hat{v}_{\alpha\beta} = [\hat{v}_\alpha \ \hat{v}_\beta]^\top$ is the reference voltage, $\hat{i}_{\alpha\beta} = [\hat{i}_\alpha \ \hat{i}_\beta]^\top$ is current injection of the converter, the angle $\kappa := \tan^{-1}(l\omega^*/r)$ models the network inductance to resistance ratio, and η, α are positive control gains. Furthermore we have

$$\mathcal{R}_2(\kappa) := \begin{bmatrix} \cos \kappa & -\sin \kappa \\ \sin \kappa & \cos \kappa \end{bmatrix}, \mathcal{K} := \frac{1}{v^{*2}} \mathcal{R}_2(\kappa) \begin{bmatrix} p^* & q^* \\ -q^* & p^* \end{bmatrix},$$

where $\mathcal{R}_2(\kappa)$ is the 2-D rotation by κ . As shown in [16] the dynamics (21) reduce to a harmonic oscillator if phase synchronization is achieved (i.e., $\mathcal{K} \hat{v}_{\alpha\beta} - \mathcal{R}_2(\kappa) \hat{i}_{\alpha\beta} = 0$) and $\|\hat{v}_{\alpha\beta}\| = v^*$ (i.e., $(v^{*2} - \|\hat{v}_{\alpha\beta}\|^2) \hat{v}_{\alpha\beta} = 0$). Rewriting (21) in polar coordinates for an inductive network (i.e., $\kappa = \pi/2$) reveals the droop characteristics (see [15]–[17]) of dVOC as

$$\dot{\theta} = \omega^* + \eta \left(\frac{p^*}{v^{*2}} - \frac{p}{\|\hat{v}_{dq}\|^2} \right), \quad (22a)$$

$$\|\dot{\hat{v}}_{dq}\| = \eta \left(\frac{q^*}{v^{*2}} - \frac{q}{\|\hat{v}_{dq}\|^2} \right) \|\hat{v}_{dq}\| + \eta \phi(v^*, \|\hat{v}_{dq}\|), \quad (22b)$$

where $\phi(v^*, \|\hat{v}_{dq}\|) = (\alpha/v^{*2}) (v^{*2} - \|\hat{v}_{dq}\|^2) \|\hat{v}_{dq}\|$. In other words, for a high voltage network and near the nominal steady state (i.e., $\|\hat{v}_{dq}\| \approx v^*$) the relationship between frequency and active power resemble that of standard droop control given in (11) with $d_\omega = \eta/v^{*2}$. Moreover, when choosing the control gain α to obtain post-fault voltages consistent with the other control algorithms described above, the first term in (22b) is negligible and (22b) reduces to the voltage regulator $\|\dot{\hat{v}}_{dq}\| \approx -2\eta\alpha (\|\hat{v}_{dq}\| - v^*)$ near the nominal steady state.

IV. NETWORK CASE STUDY

In this section we explore various performance aspects of the grid-forming control techniques in the presence of synchronous machines. In the forthcoming discussion, we use the test system shown in Figure 3. The parameters and control gains are given in Table I. The implementation in Simulink is available online [23].

In order to avoid the delay associated with the frequency measurement and signal processing introduced by standard synchronous reference frame phase-locked loop (SRF-PLL) [22], we use the mechanical frequency of the SM at node 1 in Figure 3 to evaluate the post-disturbance system frequency (e.g., in Figures 11-12). For the grid-forming converters we use the internal controller frequencies defined by (11), (13), (16) and (22). We remark that, in a real-world system and in an EMT simulation (in contrast to a phasor simulation), there is no well-defined frequency at the voltage nodes during transients, whereas the internal frequencies of the grid-forming converters are always well-defined [1, Sec. II-J], [41]. Lastly, we note that in all the forthcoming case studies we assume that the system is in steady-state at $t = 0$.

A. Performance Metrics

We adopt the standard power system frequency performance metrics i.e., maximum frequency deviation $\|\Delta\omega\|_\infty$ (i.e.,

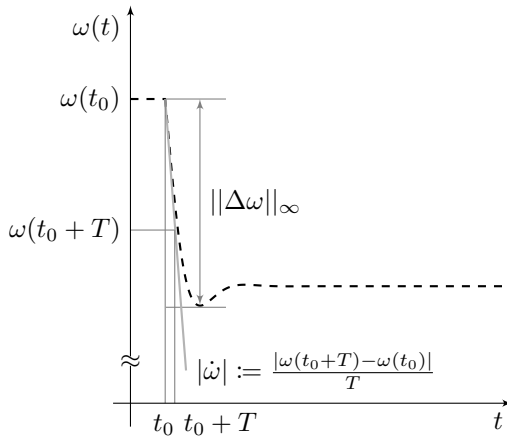


Fig. 10: Post-event frequency nadir and RoCoF.

frequency nadir/zenith) and RoCoF $|\dot{\omega}|$ (i.e., the slope of line tangent to the post-event frequency trajectory) defined by

$$||\Delta\omega||_{\infty} := \max_{t \geq t_0} |\omega^* - \omega(t)|, \quad (23a)$$

$$|\dot{\omega}| := \frac{|\omega(t_0 + T) - \omega(t_0)|}{T}, \quad (23b)$$

where $t_0 > 0$ is the time when the disturbance is applied to the system, and $T > 0$ is the RoCoF calculation window [1], [22]. See Figure 10 for visual representation of the metrics described by (23). In this work, we use $T = 250\text{ms}$, which is in line with values suggested for protection schemes (see [21, Table 1]). Dividing the metrics (23) by the size of the magnitude of the disturbance results in a measure of the system disturbance amplification.

B. Test Network Configuration and Tuning Criteria

In order to study the performance of the control approaches introduced in Section III, we apply the same strategy (with identical tuning) for both converters (i.e., at nodes 2 and 3 in Figure 3), resulting in four different SM-GFC paired models. As a benchmark, we also consider an all-SMs system with three identical SMs (i.e., at nodes 1-3). Selecting fair tuning criteria for the different control strategies is a challenging task. For this study, we tune the control parameters such that all generation units exhibit identical proportional load sharing behavior. Appendix A presents the tuning criteria and derivation of some control parameters.

C. Impact of Grid-Forming Control on Frequency Metrics

In this section, we test the system behavior for different load disturbances Δp_i . The network base load p_l is constant and uniformly distributed between nodes 5, 7 and 9 while Δp_i is only applied at node 7. For each disturbance input we calculate $||\Delta\omega_i||_{\infty}$ and $|\dot{\omega}_i|$ for the SM at node 1 and normalize these quantities by dividing by $|\Delta p_i|$. Figures 11 and 12 illustrate the distribution of system disturbance input/output gains associated with introduced frequency performance metrics. Note that the network base load p_l is 2 pu and the elements of the load disturbance sequence $\Delta p_i \in [0.2, 0.9]$, $i = 1, \dots, 100$

are uniformly increasing by 0.007 pu starting from $p_1 = 0.2$ pu.

All the grid-forming controls presented in Section III are originally designed without consideration of the converter dc and ac current limitation. Thus, to explore the intrinsic behavior of the GFCs and their influence on frequency stability the network loading scenarios described above are selected such that the GFCs dc and ac currents do not exceed the limits imposed by (3) and (7). However, in practice, GFCs are subject to strict dc and ac current limits and are combined with current limiting strategies in a modular fashion. The impact of the dc and ac current limits on the performance of GFCs is explored in Subsections IV-D to IV-F1.

Figures 11 and 12 suggest that, regardless of the choice of control strategy, the presence of grid-forming converters improves the metrics compared to the all-SM system. This possibly observation can be explained by the fast response of converters compared to the slow turbine dynamics, i.e., τ_g in (5) is larger than τ_{dc} in (2). Because of this, the converters reach frequency synchronization at a faster time-scale and then synchronize with the SM (see Figure 13). Overall, for any given disturbance input, the converters are able to react faster than the SM and the remaining power imbalance affecting the SM is smaller than in the all-SM system. This result highlights that the fast response of GFCs should be exploited instead of designing the controls of a converter (fast physical system) to emulate the slow response of synchronous machines [1].

We observe that droop control and dVOC exhibit very similar performance confirming the droop-like behavior of dVOC in predominately inductive networks (see (22)). Moreover, the difference between droop control and VSM arises from the inertial (derivative control) term in (13) and the RoCoF is considerably higher when using matching control. This can be explained by the fact that VSM, droop control, and dVOC ignore the dc voltage and aggressively regulate the ac quantities to reach angle synchronization, thus requiring higher transient peaks in dc current to stabilize the dc voltage (see Section IV-D). Although improving RoCoF, this approach can lead to instability if the converter is working close to the rated power of the dc source (but far away from its ac current limit), as shown in the next section. On the other hand, matching control regulates the dc link voltage both through the dc source and by adjusting its ac signals.

we selected the RoCoF calculation window according to the guideline [21], which accounts for noise and possible oscillations in the frequency signal. However, these guidelines were derived for a power system fully operated based on SMs. Given that grid-forming converters introduce faster dynamics, machines are expected to reach the frequency nadir faster. Hence, a smaller RoCoF windows might need to be considered in a low-inertia power system to properly assess system performance (the reader is referred to [42, Sec. III-C] for further insights on the choice of RoCoF window in a low-inertia system). We note that the performance of the different grid-forming control strategies shown in Figure 11 and 12 is sensitive to the tuning of control gains and choice of RoCoF computation window. However, due to the comparably slow response of conventional generation tech-

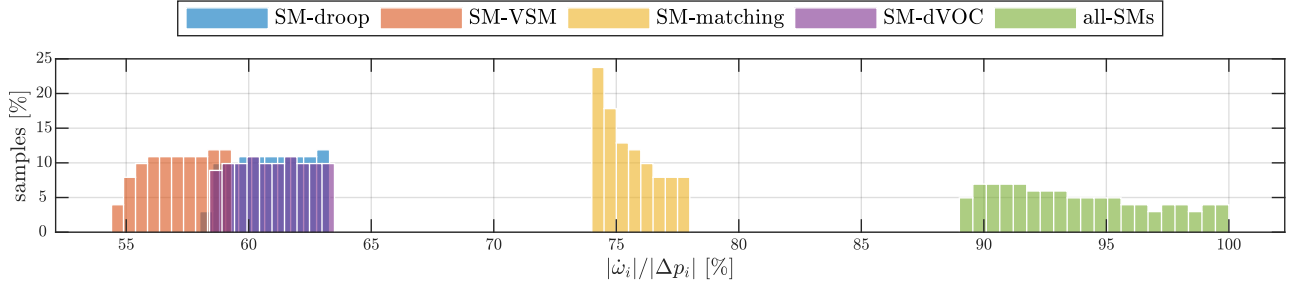


Fig. 11: Normalized distribution of the RoCoF $|\dot{\omega}_i|/|\Delta p_i|$ of the synchronous machine frequency at node 1 for load disturbances Δp_i ranging from 0.2 p.u. to 0.9 p.u. at node 7. For each load disturbance, $|\dot{\omega}_i|/|\Delta p_i|$ is normalized by the maximum value corresponding to the all-SMs configuration.

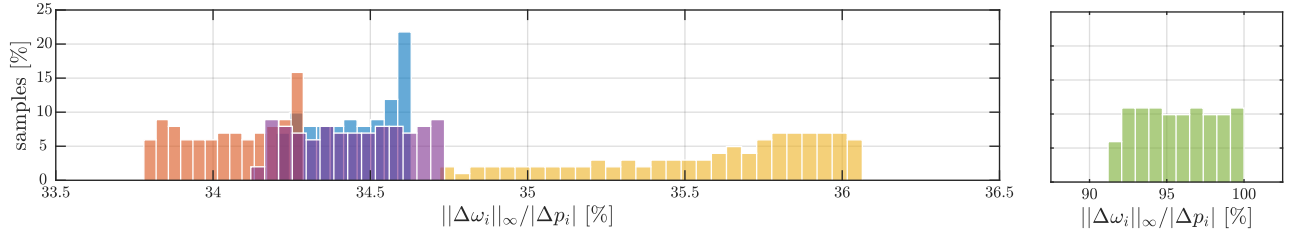


Fig. 12: Normalized distribution of the nadir $\|\Delta\omega_i\|_\infty/|\Delta p_i|$ of the synchronous machine frequency at node 1 for load disturbances Δp_i ranging from 0.2 p.u. to 0.9 p.u. at node 7. For each load disturbance, $\|\Delta\omega_i\|_\infty/|\Delta p_i|$ is normalized by the maximum value corresponding to the all-SMs configuration.

nology the performance improvements for the system with grid-forming converters over the all-SM system persist for a wide range of parameters. Moreover, using comparable tuning (see Section IV-B) the differences between the different grid-forming techniques observed in this section are expected to remain the same.

D. Response to a Large Load Disturbance

In this subsection we analyze the response of the grid-forming converters to large disturbances when the dc source is working close to its maximum rated values. Specifically, we focus on the implications of the dc current limit (3) to highlight the response of GFCs when interfacing curtailed renewable generation with low headroom (i.e., PV / wind) or a converter system with an undersized dc-dc converter stage. In such scenarios, the dc current limit can be activated independently of the ac current limit. For clarity of representation we first focus exclusively on the matching control as its angle dynamic (16) explicitly considers the dc voltage. Droop control, which does not consider the dc voltage, is solely presented to emphasize

the need for an ac current limitation mechanism to implicitly stabilize the dc voltage.

To begin with, we set the network base load p_l and load change Δp to 2.25 and 0.9 pu respectively (i.e., a total network load after the disturbance of 3.15 pu) which is equally shared by the SM and the GFCs. We expect a post-disturbance converter power injection of 1.05 pu and i_{dc} close to the dc current limit $i_{dc}^{dc} = \pm 1.2$ pu. Figure 14 shows the dc voltage and delayed dc current before saturation for the converter at node 2. For sufficiently large disturbance magnitude, i_{dc}^* and consequently i_τ exceed the current limit, i.e., the dc current $i_{dc} = i_{dc}^{dc}$ is saturated.

Figures 14 and 15 highlight that the matching control succeeds to stabilize the dc voltage despite the saturation of the dc source. The nature of matching control - which accounts for the dc-side dynamics while regulating the ac dynamics i.e., (16) - results in increased robustness with respect to large disturbances. From a circuit-theoretic point of view this is possible only if the sum of the ac power injection and filter losses equals the approximately constant dc power inflow $v_{dc} i_{dc}^{dc}$. The converter can inject constant ac power into the network only if its angle difference with respect to the remaining devices in the network is constant. In the presence of the slow SM angle and frequency dynamics this implies that the GFCs need to synchronize their frequencies to the SM so that the relative angle $\theta_{GFC} - \theta_{SM} = \theta_{max}$ is constant (see the frequency of GFC 1 following the dc source saturation at $t = 0.5$ s in Figure 15). Note that the behavior for the matching controlled GFCs is similar to that of the SM (see Section III-E and [10], [11], [13]), i.e., it achieves synchronization both under controlled or constant mechanical input power

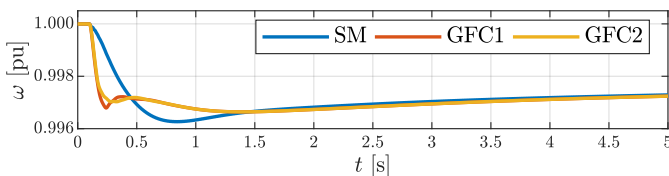


Fig. 13: Frequency of the system with two VSMs after a 0.75 pu load increase. The converters quickly synchronize with each other and then slowly synchronize with the machine.

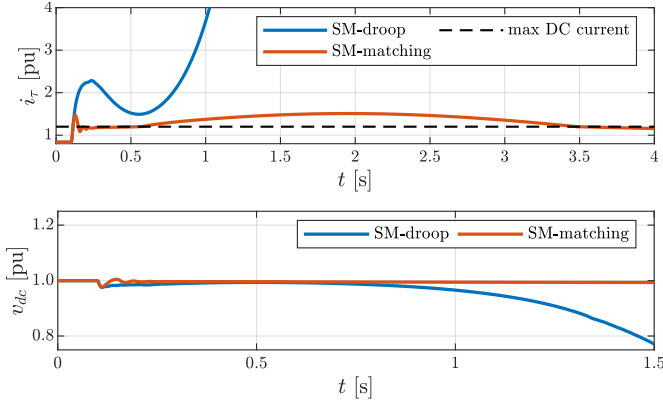


Fig. 14: dc current demand of the converter at node 2 (top) and its dc voltage (bottom) after a 0.9 pu load disturbance.

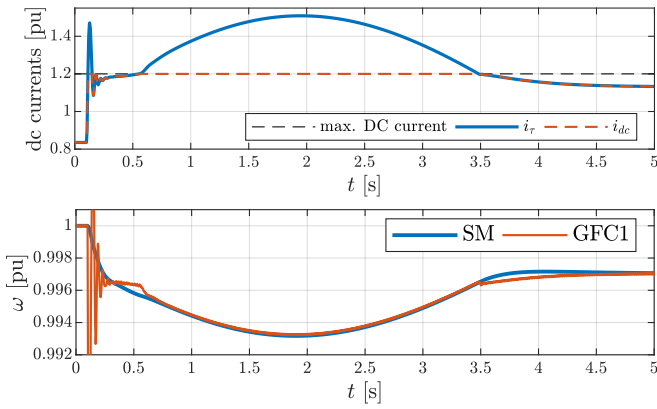


Fig. 15: dc current demand and saturated dc current (top), frequency of the converter (using matching control) at node 2 and SM after a 0.9 pu load disturbance (bottom).

(i.e., dc current injection). Figure 14 shows that for the GFCs controlled by droop control the dc-link capacitors discharge to provide $i_\tau - i_{\max}^{\text{dc}}$ (i.e., the portion of current demand which is not provided due to the saturation (3)). Because the angle and frequency dynamics (i.e., (11), (13), and (22a)) of droop control, VSM, and dVOC purely rely on ac measurements they are agnostic to the dc dynamics and source saturation. Consequently, a prolonged duration of dc source saturation results in a collapse of the dc voltage. A potential remedy is to incorporate an ac current limitation scheme to prevent the GFC from depleting the dc-link capacitor. This observation motivates the discussion in the next subsection with restricted focus on droop control, VSM, and dVOC techniques.

E. Incorporating the AC Current Limitation

In this subsection, we investigate if the ac current limitation (7) presented in section III-A can mitigate the instabilities of the GFCs controlled by droop control, VSM and dVOC under dc source saturation. To this end, we consider the same base load and disturbance as in previous test case, i.e., $p_l = 2.25$ and $\Delta p = 0.9$ pu. For this scenario, the GFCs dc transient current demand i_τ and the switching node current magnitude $\|\dot{i}_{s,dq}\|$ exceeds the limits (i.e., $i_{\max}^{\text{dc}} = i_{\max}^{\text{ac}} = 1.2$ pu) imposed by (3) and (7).

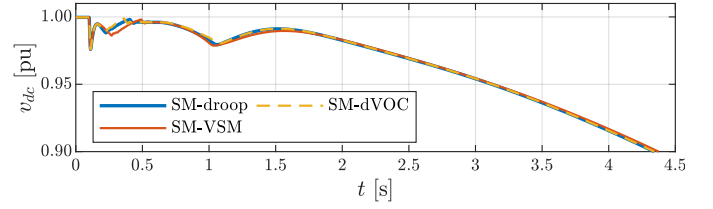


Fig. 16: dc voltage of the converter at node 2 after a 0.9 pu load disturbance when both dc and ac limitation schemes (3) and (7) are active and $\tau_g = 5$ s.

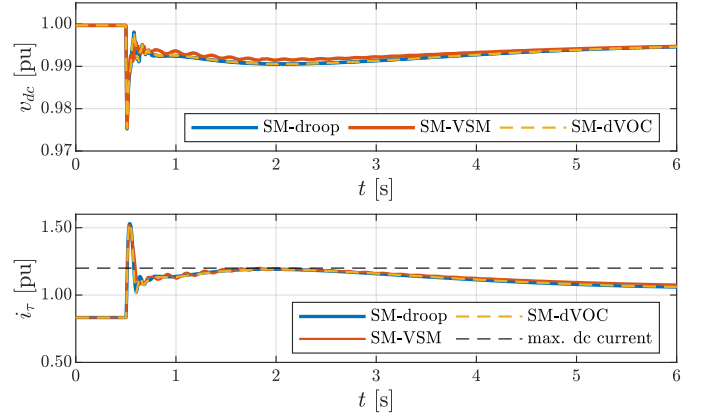


Fig. 17: dc voltage (top) and dc current demand (bottom) of the converter at node 2 after a 0.9 pu load disturbance when all the limitation schemes i.e., (3), (7) and (24) are active and $\tau_g = 5$ s.

We observe that using the ac current limiter does not stabilize the dc voltage of the GFCs controlled by droop control, VSM, and dVOC. Figure 16 illustrates the behavior of the GFC at node 2. Specifically, the current limitation imposed by (7) results in integrator windup, a loss of ac voltage control and, ultimately, instability of the grid-forming control [34] and dc voltage. We remark that GFCs exhibit the same instability behavior when the ac current limit is smaller than that of the dc-side i.e., $i_{\max}^{\text{ac}} < i_{\max}^{\text{dc}}$.

To mitigate this load-induced instability, we explore a current limitation scheme that modifies the active power set-point when $\|\dot{i}_{s,dq}\|$ exceeds a certain threshold value, i.e.,

$$\Delta p^* := \begin{cases} 0 & \text{if } \|\dot{i}_{s,dq}\| \leq i_{\text{th}}^{\text{ac}}, \\ \gamma_p (\|\dot{i}_{s,dq}\| - i_{\text{th}}^{\text{ac}}) & \text{if } \|\dot{i}_{s,dq}\| > i_{\text{th}}^{\text{ac}}, \end{cases} \quad (24)$$

and Δp^* is added to p^* in (10), (11), (13b) and (21), γ_p denotes a proportional control gain, and $i_{\text{th}}^{\text{ac}} < i_{\max}^{\text{ac}}$ is the activation threshold. Note that the control law (24) implicitly manipulates the grid-forming dynamics through their set-points such that the ac current magnitude stays within the admissible limits for large increases in load. We emphasize that this strategy aims at mitigating instabilities induced by large load increases and that the resulting GFC response to grid faults needs to be carefully studied.

For a 0.9 pu load increase, the current limitation strategy (24) is able to stabilize the system with $i_{\text{th}}^{\text{ac}} = 0.9$ pu and $\gamma_p = 2.3 (p_b / i_b^{\text{ac}})$ where p_b and i_b^{ac} denote the converter base power

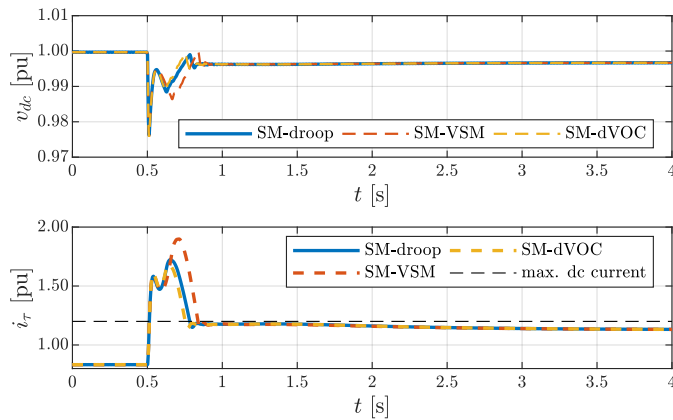


Fig. 18: dc voltage (top) and dc current demand (bottom) of the converter at node 2 after a 0.9 pu load disturbance when both dc and ac limitation schemes (3) and (7) are active and $\tau_g = 1$ s.

and current, respectively. Figure 17 depicts the response of the same GFC as in Figure 16. Note that (24) effectively stabilizes the dc voltage for droop control, VSM, and dVOC. Moreover, in contrast to Figure 14, after the post-disturbance transient the dc source is no longer in saturation. Broadly speaking, this strategy succeeds to stabilize the system by steering the GFC power injection away from the critical limits. However, this also influences the post-disturbance operating point of the GFCs due to the threshold value being below the rated value.

Finally, we observe that the different time-scales in a low-inertia system contribute to the instabilities observed in the previous section. In particular, if the SM's turbine responds faster, GFCs with the standard limitation strategy (7) preserve stability - without the need to implement (24) - despite the fact that transient dc and ac currents exceed the limits. Figure 18 shows the GFCs responses when the SM turbine delay τ_g is 1s (cf. Figure 16 where $\tau_g = 5$ s). It can be seen that the slow SM turbine dynamics again contribute to the system instability when dc and ac currents are saturated. We conclude that the presence of different time-scales in a low-inertia system - often neglected in the literature [26], [33]–[39] - must be considered in designing a robust ac current limitation mechanism for the GFCs.

Remark 2. (dc and ac measurements)

We observe that using ac measurements to drive the angle dynamics - e.g., VSMs use active power measurements in (13) - improves the frequency performance of GFCs (see Figures 11 and 12). On the other hand, using dc voltage measurements - e.g., matching control (16) - results in robustness with respect to dc current limits. Further research is required to combine these complementary benefits by using both dc and ac measurements in grid-forming control.

F. Interaction of GFC and SM Dynamics

The forthcoming discussion highlights that the interplay between the fast GFC and slow SM dynamics influences the system stability. The following case studies are tightly related to the scenarios in previous subsections.

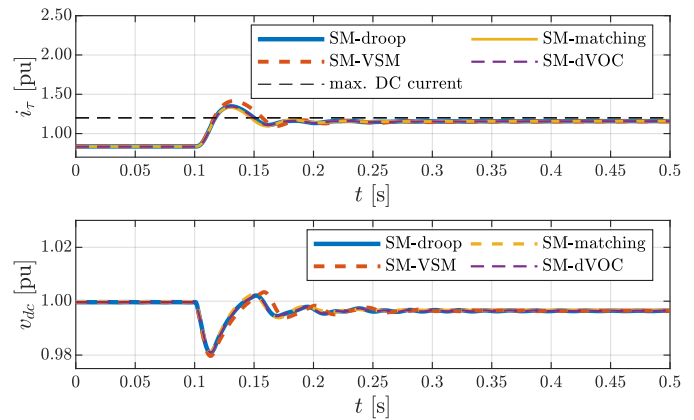


Fig. 19: dc current demand (top) and dc voltage (bottom) of the converter at node 2 after loss of the SM at node 1.

1) *Loss of synchronous machine:* we study the response of GFCs when disconnecting the SM at node 1, that is, the system turns into an all-GFCs network. The implications of such a contingency are threefold. First, the power injected by the machine, which partially supplies the base load, is no longer available. Second, the stabilizing dynamics associated with the machine's governor, AVR, and PSS are removed from the system. Third, the slow dynamics of the SM no longer interact with the fast dynamics of the GFCs.

For this test, we set the base load to 2.1 pu, and the SM and GFCs set-points are set to 0.6 and 0.75 pu respectively. Note that when the SM at node 1 is disconnected, the converters increase their power output according to the power sharing behavior inherent to all four grid-forming controls (see Appendix A). The resulting increase in the converter power injection to roughly 1.05 pu is similar to the load disturbance scenario used to illustrate the instability behavior of droop control in Figure 14. Figure 19 shows i_τ and v_{dc} for the converter at node 2. Although the disturbance magnitude affecting the converters is similar to the one in studied in Subsection IV-D, all GFCs remain stable after the loss of the SM without the need to incorporate (24). In particular, due to the absence of the slow turbine dynamics and fast synchronization of the converters i_τ exceeds the limit $i_{dc_max}^{dc}$ for around 50ms while it remains above the limit for a prolonged period of time in Figure 14.

This highlights the problematic interaction between the fast response of the GFCs and the slow response of the SM. While the synchronous machine perfectly meets classic power system control objectives on slower time scales, the dominant feature of GFCs is their fast response. However, the fast response of GFCs can also result in unforeseen interactions with other parts of the system such as the slow SM response (shown here), line dynamics (see [16], [29]), and line limits [43].

2) *Low-inertia vs. no-inertia systems:* considering the same load disturbance scenario as in Subsection IV-D, we observe the same instability of droop control when the test system contains one GFC and two SMs, i.e., the instability cannot be prevented by adding more inertia to the system.

Figure 20 shows the dc current demand i_τ (i.e., before saturation) and dc voltage in an all-GFCs (i.e., no-inertia)

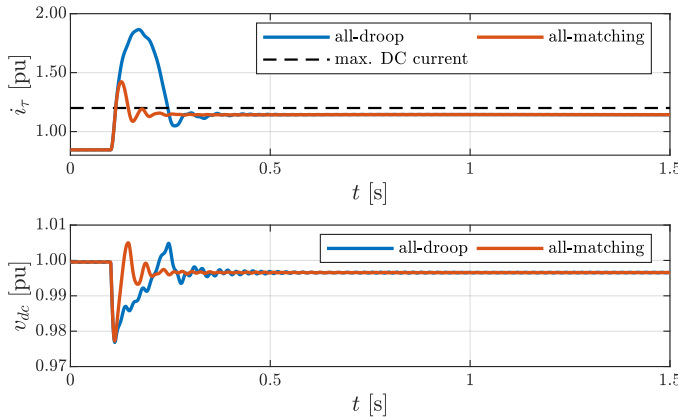


Fig. 20: dc current demand (top) and dc voltage (bottom) after a 0.9 pu load disturbance in an all-GFC system.

system for a load increase of $\Delta p = 0.9$ pu. In this case, the GFCs quickly synchronize to the post-event steady state, which does not exceed the maximum dc current, saturate the dc source for only approximately 200ms, and remain stable. In contrast, in the system with two GFCs and one SM, the SM does not reach its increased post-event steady-state power injection for several seconds. During this time the response of droop control results in a power injection that exceeds the limits of the dc source and collapses the dc voltage. In other words, the slow response of the SM due to the large turbine time constant prolongs the duration of dc source saturation for the GFCs which results in depleting the dc-link if the converter ac current is not limited. We conclude this subsection by remarking that in the mixed SM-GFCs system in the Subsections IV-D and IV-E, it is vital to account for dc side limits (either through ac current limits or dc voltage measurements) to stabilize the GFCs in presence of SMs. However, in an all-GFC system - either by default or due to the loss of SM - the dc side is only limited briefly and the system remains stable. This observation highlights that the interaction of the fast GFC dynamics and slow SM dynamics can potentially contribute to system instability.

V. QUALITATIVE ANALYSIS

In this section, we provide a qualitative but insightful analysis that explains the results observed in Section IV-C and Section IV-D. To this end, we develop simplified models that capture the small-signal frequency dynamics of synchronous machines and grid-forming converters. Applying arguments from singular perturbation theory [12], [44] results in a model that highlights the main salient features of the interaction of synchronous machines and grid-forming converters.

A. Frequency dynamics incorporating GFCs

To obtain a simplified model of the frequency dynamics of the GFCs, we assume that the cascaded ac voltage and ac current control (see (6) and (8)) achieve perfect tracking (i.e., $\mathbf{v}_{dq} = \hat{\mathbf{v}}_{dq}$). Assuming that the system operates near the nominal steady-state (i.e., $\|\mathbf{v}_{dq}\| \approx v^*$, $\omega \approx \omega^*$) and $p^* = 0$,

$q^* = 0$, we rewrite the remaining dynamics in terms of the voltage angle and power injection at every bus. This results in a simplified model of the angle θ and the frequency ω of a GFC or SM relative to a frame rotating at the nominal frequency ω^* .

1) *Droop control and dVOC*: For a converter controlled by droop control or dVOC, we obtain

$$\dot{\theta} = -d_\omega p, \quad (25)$$

where p is the power flowing out of the converter and d_ω is the droop control gain and given by $d_\omega = \eta/v^{*2}$ for dVOC.

2) *Synchronous machine, VSM, and matching control*: For a synchronous machine, a VSM, and a converter controlled by matching control we obtain

$$\dot{\theta} = \omega, \quad (26a)$$

$$2H\dot{\omega} = -D\omega + \text{sat}(p_\tau, p_{\max}) - p, \quad (26b)$$

$$\tau \dot{p}_\tau = -p_\tau - d_p \omega. \quad (26c)$$

For a SM the parameters directly correspond to the parameters of the machine model presented in Section II-B, i.e., H , d_p , and $\tau = \tau_g$, are the machine inertia constant, governor gain, and turbine response time, and the model does not capture SM losses (i.e., $D = 0$) or damper winding torques. Throughout this work we have not considered a limit on the turbine power output (i.e., $p_{\max} = \infty$) because a synchronous machine, in contrast to a GFC, typically has sufficient reserves to respond to the load changes and faults considered in this work. For the VSM presented in Section III-D, we obtain $\tau = 0$, $p_\tau = 0$, $H = 1/2J\omega^*$, and $D = D_p\omega^*$, i.e., the VSM does not emulate a turbine and implements no saturation of the damping term in its frequency dynamics (13b). Finally, for matching control we obtain $\tau = \tau_{dc}$, $p_{\max} = v_{dc}^* i_{\max}^{dc}$, $H = 1/2C_{dc}/k_\theta^2$, $d_p = k_{dc}/k_\theta$ (see Section III-E) and $D = 0$, i.e., by linking frequency and dc voltage, matching control clarifies that the dc source plays the role of the turbine in a machine and the proportional dc voltage control plays the role of a governor.

B. Reduced-order model

For brevity of the presentation we will now restrict our attention to the case of one SM and one GFC. The equivalent inertia constants and turbine time constants for the different grid-forming converter control strategies are either zero or negligible compared to typical inertia constants and turbine time constants for machines (see Table I). We therefore, assume that the states of the synchronous machine are slow variables, while the states of the GFC are fast and apply ideas from singular perturbation theory [12], [44].

Using the dc power flow approximation and $p_{d,\text{GFC}}$ and $p_{d,\text{SM}}$ to denote a disturbance input, we obtain $p_{\text{GFC}} = b(\theta_{\text{GFC}} - \theta_{\text{SM}}) + p_{d,\text{GFC}}$ and $p_{\text{SM}} = b(\theta_{\text{SM}} - \theta_{\text{GFC}}) + p_{d,\text{SM}}$, where b is the line susceptance. Neglecting the frequency dynamics and dc source dynamics, i.e., letting $\tau \rightarrow 0$ and $H \rightarrow 0$, the dynamics of the relative angle $\delta = \theta_{\text{SM}} - \theta_{\text{GFC}}$ are given by $\dot{\delta} = \omega_{\text{SM}} - (D_{\text{GFC}} + d_{p,\text{GFC}})(b\delta - p_{d,\text{GFC}})$ if $|d_{p,\text{GFC}}| < |p_{\max}|$, $\dot{\delta} = \omega_{\text{SM}} - D_{\text{GFC}}(b\delta - p_{d,\text{GFC}} \pm p_{\max})$ if the dc source is saturated, and D_{GFC} denotes the damping provided by the GFC. For typical droop gains and network

parameters, the relative angle dynamics are fast compared to the machine dynamics. Letting $\dot{\delta} \rightarrow 0$, we obtain the reduced-order model

$$2H\dot{\omega}_{SM} = -\text{sat}(D_{GFC}\omega_{SM}, p_{\max}) + p_{\tau,SM} + p_d, \quad (27a)$$

$$\tau\dot{p}_{\tau,SM} = -p_{\tau,SM} - d_p\omega_{SM}. \quad (27b)$$

where $p_d = p_{d,GFC} + p_{d,SM}$, H , d_p , and τ are the inertia constant, governor gain, and turbine time constant of the synchronous machine, D_{GFC} is the damping provided by the GFC, i.e., $D_{GFC} = 1/d_\omega$ (droop, dVOC, VSM) or $D_{GFC} = d_p$ (matching). Moreover, droop control, dVOC, and the VSM implement no saturation of their power injection in their respective angle / frequency dynamics (i.e., (11b), (22a), and (13b)) resulting in $p_{\max} = \infty$. In contrast, for matching control the saturation of the dc source results in $p_{\max} = v_{dc}^* i_{\max}^*$.

We note that for the case of under damped dynamics (27) and without saturation, a closed-form expression for the step response and frequency nadir (27) can be found in [19, Sec. V-A]. However, even for the seemingly simple model (27) the dependence of the nadir on the parameters is very involved and does not provide much insight. By neglecting the damping term in (27a) and the feedback term $-p_{\tau,SM}$ in (27b) an insightful expression for the nadir is obtained in [45]. However, the key feature of the GFCs is that they contribute damping, which is not captured by analysis in [45]. Nonetheless, the model (27) provides several insights that we discuss in the next section.

C. Impact of Grid-Forming Control on Frequency Stability

A system with three synchronous machines as in Section IV can be modeled by (27) with $H = 3H_{SM}$, $d_p = 3d_{p,SM}$, $\tau = \tau_{SM}$ and $D_{GFC} = 0$. This corresponds to the well known *center of inertia* frequency model with first-order turbine dynamics (see [3], [19]). In contrast, if two SMs are replaced by GFCs with equal droop setting we obtain $H = H_{SM}$, $d_p = d_{p,SM}$, $\tau = \tau_{SM}$ and $D_{GFC} = 2d_{p,SM}$.

This highlights that, on the time-scales of the SM, the GFCs provide fast acting frequency control. After an increase in load the machine inertia serves as buffer until the relatively slow turbine provides additional power to the machine. In contrast, the converters respond nearly instantaneously to any imbalance and therefore the need for inertia is decreased. Intuitively, this increase in fast primary frequency control should result in lower nadir values. Similarly, the additional damping provided by the converter in (27) can be interpreted as a filter acting on the power imbalance, i.e., the GFCs are providing $D_{GFC}\omega_{SM}$ or p_{\max} and the power imbalance affecting the machine is reduced, therefore resulting in smaller average RoCoF.

To validate the model (27) and our interpretation, we compute the frequency nadir and averaged RoCoF (see (23)) for the machine parameters and disturbance used in in Section IV, and $H = \nu 3H_{SM}$, $d_p = \nu 3d_{p,SM}$, $\tau = \tau_{SM}$ and $D_{GFC} = (1 - \nu)d_{p,SM}$ and $D = 0$, where $\nu \in [1/3, 1]$ is a scalar parameter that interpolates the parameters between the two cases (all SM, one SM and two GFCs). The average RoCoF and frequency nadir according to (27) are shown in Figure 21. The case with $p_{\max} = 1.2$ corresponds to matching

control, the one with $p_{\max} = \infty$ to droop control, dVOC, and VSMs. It can be seen that the GFCs result in an improvement compared to the all SM scenario, that the implicit saturation of the power injection by matching control results in a smaller improvement compared to droop control, dVOC and VSMs, and that the reduction in the average RoCoF and frequency nadir is line with the corresponding results in Figure 11 and Figure 12.

D. Instability in the presence of large load disturbance

The instabilities of droop control, dVOC, and the VSM observed in Section IV-D can qualitatively be investigated using a simplified model of the dc-side. To compute the power $v_{dc}i_x$ flowing out of the dc-link capacitor, we assume that the controlled converter output filter dynamics are fast and can be neglected (i.e., $\dot{i}_{s,\alpha\beta} = 0$, $\dot{v}_{\alpha\beta} = 0$) and that the ac output filter losses are negligible. This results in $v_{dc}i_x = \mathbf{v}_{s,\alpha\beta}^T \dot{i}_{s,\alpha\beta} = \mathbf{v}_{\alpha\beta}^T \dot{i}_{\alpha\beta} = p$. Moreover, we neglect the dc source dynamics to obtain the simplified dc voltage dynamics

$$C_{dc}\dot{v}_{dc} = -G_{dc}v_{dc} + \text{sat}(k_{dc}(v_{dc}^* - v_{dc}), i_{\max}^{dc}) - \frac{p}{v_{dc}}, \quad (28)$$

i.e., the active power p flowing into the grid is drawn from the dc-link capacitor that is stabilized by a proportional control (see (10)) if the dc current i_τ is not saturated. For a large enough constant perturbation $p > 0$ the dc current in (28) becomes saturated and controllability of the voltage v_{dc} is lost and the dc voltage becomes unstable.

In other words, if the dc source is saturated the power p has to be controlled to stabilize the dc voltage. Matching control achieves this through the angle dynamics $\dot{\theta} = k_\theta v_{dc}$ which converge to a constant angle difference (i.e., $\omega_{SM} = \omega_{GFC}$) and power injection when the dc source is saturated and the SM has enough reserves to maintain $\omega_{SM} \approx \omega^*$ with the GFC providing its maximum output power. Moreover, for matching control it can be verified that $(\omega_{GFC} - \omega^*)/\omega^* = (v_{dc} - v_{dc}^*)/v_{dc}^*$.

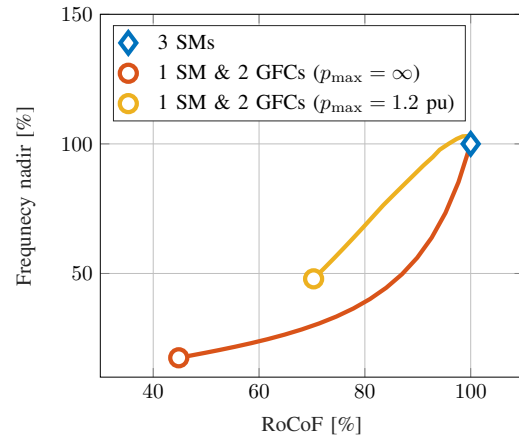


Fig. 21: Change in averaged RoCoF and frequency nadir when transitioning from a system with 3 SMs to a system with one SM and two GFCs.

Therefore, the dc voltage deviation is proportional to the frequency deviation and the GFC with matching control remains stable for the scenario shown in Section IV-D.

VI. SUMMARY AND FURTHER WORK

In this paper we provided an extensive review of different grid-forming control techniques. Subsequently, we used the IEEE 9-bus test system incorporating high-fidelity GFC and SM models to investigate the performance of different control techniques and their interaction with SM. Our case studies revealed that 1) the presence of the GFCs improves the frequency stability metrics compared to the baseline all-SMs system, 2) under a sufficiently large load disturbance, it is vital to implement an ac current limiting scheme to stabilize the grid-forming techniques which only rely on the ac measurements, 3) matching control exhibits robustness to the dc source saturation since its angle dynamics takes into account the dc quantities, 4) we explored the stabilizing influence of the ac current limitation, and 5) we investigated the behavior of GFCs in response to the loss of SM and in all-GFCs system highlighting a potentially destabilizing interaction between the GFCs and SMs dynamics. Moreover, we provided a qualitative analysis of GFCs impact on the frequency stability. Topics for the future works include 1) further exploration of the impacts of dc and ac current limitations on the GFCs behavior and providing a formal stability analysis, 2) proposing a complete ac current limitation strategy which is robust to load-induced over-current as well as grid faults, 3) the seamless transition between grid-forming and grid-following operation, and 4) blending of the different control strategies into a controller that achieves their complementary benefits.

APPENDIX A TUNING CRITERIA

The load-sharing capability of the control techniques presented in Section III is investigated in [4], [7], [15]. Considering a heterogeneous network consisting of several GFCs (with different control) and SMs, we tune the control parameters such that all the units exhibit identical proportional load-sharing in steady-state. For the SM and droop controlled GFC, (5a) and (11b) can be rearranged to

$$\omega^* - \omega = \frac{1}{d_p} (p - p^*), \quad (29a)$$

$$\omega^* - \omega = d_\omega (p - p^*). \quad (29b)$$

For VSM, assuming steady-state frequency and setting $\ddot{\theta} = \dot{\omega} = 0$ in (13b) results in

$$\omega^* - \omega = \frac{1}{D_p \omega^*} (p - p^*). \quad (30)$$

For matching control, we assume that in steady-state $i_{dc} \approx i_{dc}^*$ and $v_{dc}/v_{dc}^* \approx 1$. Setting $\dot{\omega} = 0$ in (19b) and replacing i_{dc} by the expression from (10) yields

$$\omega^* - \omega = \frac{k_\theta}{k_{dc} v_{dc}} (p - p^*). \quad (31)$$

Lastly for dVOC, assuming $\|\hat{v}_{dq}\| \approx v^*$ in steady-state, the angle dynamics (22a) becomes

$$\omega^* - \omega = \frac{\eta}{v^{*2}} (p - p^*). \quad (32)$$

Hence, for any given droop gain d_p , if d_ω, D_p, k_{dc} and η are selected such that the slopes of (29)-(32) are equal, all the GFC control techniques and SM perform equal-load sharing. Moreover, by selecting k_{dc} based on this criteria, the dc voltage control gain in (10) is automatically set which is identical for all GFC implementation [23].

Regarding the ac voltage regulation, the control gains in (12), (15), (17), and (22b) are selected to regulate the ac voltage at approximately equal time-scales. We refer to [46] for details on tuning the cascaded inner loops presented in Subsection III-A. It is noteworthy, that the time-scale of the reference model (i.e., grid-forming dynamics) must be slower than ac voltage control shown in Figure 4 to ensure optimal performance. Similarly, the ac current control must be faster than the outer voltage controller. Lastly, the choice of virtual inertia constant in (13b) can largely influence VSM's dynamic behavior. We adopted the recommendation $J/D_p = 0.02$ proposed in [8]. The parameters used in the implementation [23] are reported in Table I.

TABLE I: Case study model and control parameters [23].

IEEE 9-bus test system base values					
S_b	100 MVA	v_b	230 kV	ω_b	$2\pi 50$ rad/s
MV/HV transformer					
S_t	210 MVA	v_1	13.8 kV	v_2	230 kV
$R_1 = R_2$	0.0027 pu	$L_1 = L_2$	0.08 pu	$R_m = L_m$	500 pu
single LV/MV transformer module in Figure 2					
S_t	1.6 MVA	v_1	1 kV	v_2	13.8 kV
$R_1 = R_2$	0.0073 pu	$L_1 = L_2$	0.018 pu	R_m, L_m	347, 156 pu
synchronous machine (SM)					
S_t	100 MVA	v_t	13.8 kV	D_f	0
H	3.7 s	d_p	1 %	τ_g	5 s
single converter module in Figure 2					
S_t	500 kVA	G_{dc}, C_{dc}	$0.83, 0.008 \Omega^{-1}, F$	v_{dc}^*, v_{ll-rms}^*	2.44, 1 kV
R	0.001 Ω	L	200 μH	C	300 μF
n	100	τ_{dc}	50 ms	i_{max}^{dc}	1.2 pu
ac current, ac voltage, and dc voltage control					
$k_{v,p}, k_{v,i}$	0.52, 232.2	$k_{i,p}, k_{i,i}$	0.73, 0.0059	k_{dc}	1.6×10^3
droop control					
d_ω	$2\pi 0.05$ rad/s	ω^*	$2\pi 50$	k_p, k_i	0.001, 0.5
virtual synchronous machine (VSM)					
D_p	10^5	J	2×10^3	k_p, k_i	0.001, 0.0021
matching control					
k_θ	0.12	k_{dc}	1.6×10^3	k_p, k_i	0.001, 0.5
dispatchable virtual oscillator control (dVOC)					
η	0.021	α	6.66×10^4	κ	$\pi/2$

REFERENCES

- [1] F. Milano, F. Dörfler, G. Hug, D. J. Hill, and G. Verbič, "Foundations and challenges of low-inertia systems," in *Power Systems Computation Conference (PSCC)*, 2018.
- [2] P. W. Sauer and M. A. Pai, *Power system dynamics and stability*. Prentice hall, 1998.
- [3] P. Kundur, *Power system stability and control*. McGraw-Hill, 1994.
- [4] A. Tayyebi, F. Dörfler, F. Kupzog, Z. Miletic, and W. Hribernik, "Grid-forming converters – inevitability, control strategies and challenges in future grid applications," in *CIREP Workshop*, 2018.
- [5] "High penetration of power electronic interfaced power sources (hppeips) ENTSO-E guidance document for national implementation for network codes on grid connection," ENTSO-E, Tech. Rep., 2017.

- [6] M. Chandorkar, D. Divan, and R. Adapa, "Control of parallel connected inverters in standalone AC supply systems," *IEEE Trans. Ind. Appl.*, vol. 29, no. 1, pp. 136–143, 1993.
- [7] S. D'Arco, J. A. Suul, and O. B. Fosso, "A virtual synchronous machine implementation for distributed control of power converters in smart grids," *Electric Power Systems Research*, vol. 122, pp. 180–197, 2015.
- [8] Q. C. Zhong and G. Weiss, "Synchronverters: Inverters that mimic synchronous generators," *IEEE Trans. Ind. Electron.*, vol. 58, no. 4, pp. 1259–1267, 2011.
- [9] Q. Zhong, P. Nguyen, Z. Ma, and W. Sheng, "Self-synchronized synchronverters: Inverters without a dedicated synchronization unit," *IEEE Trans. Power Electron.*, vol. 29, no. 2, pp. 617–630, 2014.
- [10] I. Cvetkovic, D. Boroyevich, R. Burgos, C. Li, and P. Mattavelli, "Modeling and control of grid-connected voltage-source converters emulating isotropic and anisotropic synchronous machines," in *IEEE Workshop on Control and Modeling for Power Electronics (COMPEL)*, 2015.
- [11] C. Arghir, T. Jouini, and F. Dörfler, "Grid-forming control for power converters based on matching of synchronous machines," *Automatica*, vol. 95, pp. 273–282, 2018.
- [12] S. Curi, D. Groß, and F. Dörfler, "Control of low-inertia power grids: A model reduction approach," in *IEEE Conference on Decision and Control (CDC)*, 2017, pp. 5708–5713.
- [13] C. Arghir and F. Dörfler, "The electronic realization of synchronous machines: model matching, angle tracking and energy shaping techniques," *IEEE Trans. Power Electron.*, 2019.
- [14] M. Sinha, F. Dörfler, B. B. Johnson, and S. V. Dhople, "Uncovering droop control laws embedded within the nonlinear dynamics of van der pol oscillators," *IEEE Trans. Control Netw. Syst.*, vol. 4, no. 2, pp. 347–358, 2017.
- [15] M. Colombino, D. Gross, J. Brouillon, and F. Dörfler, "Global phase and magnitude synchronization of coupled oscillators with application to the control of grid-forming power inverters," *IEEE Trans. Autom. Control*, 2019.
- [16] D. Groß, M. Colombino, J.-S. Brouillon, and F. Dörfler, "The effect of transmission-line dynamics on grid-forming dispatchable virtual oscillator control," *IEEE Trans. Control Netw. Syst.*, 2019, to appear.
- [17] G. Seo, I. Subotic, B. Johnson, M. Colombino, D. Groß, and F. Dörfler, "Dispatchable virtual oscillator control for decentralized inverter-dominant power systems - analysis of droop characteristic and verification," in *Applied Power Electronics Conference (APEC)*, 2018.
- [18] N. Pogaku, M. Prodanovic, and T. C. Green, "Modeling, analysis and testing of autonomous operation of an inverter-based microgrid," *IEEE Trans. Power Electron.*, vol. 22, no. 2, pp. 613–625, 2007.
- [19] F. Paganini and E. Mallada, "Global analysis of synchronization performance for power systems: bridging the theory-practice gap," *IEEE Trans. Autom. Control*, 2019.
- [20] M. Pirani, J. W. Simpson-Porco, and B. Fidan, "System-theoretic performance metrics for low-inertia stability of power networks," in *IEEE Conference on Decision and Control (CDC)*, 2017, pp. 5106–5111.
- [21] RG-CE System Protection & Dynamics Sub Group, "Frequency measurement requirements and usage," ENTISO-E, Tech. Rep., 2018.
- [22] B. K. Poolla, D. Groß, and F. Dörfler, "Placement and implementation of grid-forming and grid-following virtual inertia and fast frequency response," *IEEE Trans. Power Syst.*, vol. 34, no. 4, pp. 3035–3046, 2019.
- [23] A. Tayyebi, D. Groß, and A. Anta, "GridFormingConverters: Implementation of grid-forming control techniques in IEEE 9-bus system," Git repository, 2019, <https://github.com/ATayyebi/GridFormingConverters>.
- [24] U. Markovic, O. Stanojev, E. Vrettos, P. Aristidou, and G. Hug, "Understanding stability of low-inertia systems," *engrXiv preprint*, 2019, Available at <http://engrxiv.org/jwzrq>.
- [25] A. Yazdani and R. Iravani, *Voltage-sourced converters in power systems*. Wiley Online Library, 2010.
- [26] G. Denis, T. Prevost, M. Debry, F. Xavier, X. Guillaud, and A. Menze, "The Migrate project: the challenges of operating a transmission grid with only inverter-based generation. A grid-forming control improvement with transient current-limiting control," *IET Renewable Power Generation*, vol. 12, no. 5, pp. 523–529, 2018.
- [27] *IEEE recommended practice for excitation system models for power system stability studies*, IEEE Std. 421.5, 2016.
- [28] R. D. Zimmerman, C. E. Murillo-Sanchez, and R. J. Thomas, "MATPOWER: Steady-state operations, planning, and analysis tools for power systems research and education," *IEEE Trans. Power Syst.*, pp. 12–19, 2011.
- [29] P. Vorobev, P. Huang, M. A. Hosani, J. L. Kirtley, and K. Turitsyn, "High-fidelity model order reduction for microgrids stability assessment," *IEEE Trans. Power Syst.*, vol. 33, no. 1, pp. 874–887, 2018.
- [30] V. Purba, S. V. Dhople, S. Jafarpour, F. Bullo, and B. B. Johnson, "Reduced-order structure-preserving model for parallel-connected three-phase grid-tied inverters," in *IEEE Workshop on Control and Modeling for Power Electronics (COMPEL)*, 2017.
- [31] M. M. S. Khan, Y. Lin, B. Johnson, V. Purba, M. Sinha, and S. Dhople, "A reduced-order aggregated model for parallel inverter systems with virtual oscillator control," in *IEEE Workshop on Control and Modeling for Power Electronics (COMPEL)*, 2018.
- [32] V. Purba, B. B. Johnson, M. Rodriguez, S. Jafarpour, F. Bullo, and S. V. Dhople, "Reduced-order aggregate model for parallel-connected single-phase inverters," *IEEE Trans. Energy Convers.*, vol. 34, no. 2, pp. 824–837, 2019.
- [33] M. G. Taul, X. Wang, P. Davari, and F. Blaabjerg, "Current limiting control with enhanced dynamics of grid-forming converters during fault conditions," *IEEE Trans. Emerg. Sel. Topics Power Electron.*, 2019.
- [34] H. Xin, L. Huang, L. Zhang, Z. Wang, and J. Hu, "Synchronous instability mechanism of P-f droop-controlled voltage source converter caused by current saturation," *IEEE Trans. Power Syst.*, vol. 31, no. 6, pp. 5206–5207, 2016.
- [35] X. Wang, Y. W. Li, F. Blaabjerg, and P. C. Loh, "Virtual-impedance-based control for voltage-source and current-source converters," *IEEE Trans. Power Electron.*, vol. 30, no. 12, pp. 7019–7037, 2015.
- [36] Q. Zhong and G. C. Konstantopoulos, "Current-limiting droop control of grid-connected inverters," *IEEE Trans. Ind. Electron.*, vol. 64, no. 7, pp. 5963–5973, 2017.
- [37] A. Gkoutaras, S. Dieckerhoff, and T. Sezi, "Evaluation of current limiting methods for grid forming inverters in medium voltage microgrids," in *2015 IEEE Energy Conversion Congress and Exposition (ECCE)*, 2015, pp. 1223–1230.
- [38] I. Sadeghkhani, M. E. Hamedani Golshan, J. M. Guerrero, and A. Mehrizi-Sani, "A current limiting strategy to improve fault ride-through of inverter interfaced autonomous microgrids," *IEEE Trans. Smart Grid*, vol. 8, no. 5, pp. 2138–2148, 2017.
- [39] A. D. Paquette and D. M. Divan, "Virtual impedance current limiting for inverters microgrids with synchronous generators," *IEEE Trans. Ind. Appl.*, vol. 51, no. 2, pp. 1630–1638, 2015.
- [40] L. Huang, H. Xin, Z. Wang, K. Wu, H. Wang, J. Hu, and C. Lu, "A virtual synchronous control for voltage-source converters utilizing dynamics of DC-link capacitor to realize self-synchronization," *IEEE Trans. Emerg. Sel. Topics Power Electron.*, vol. 5, no. 4, pp. 1565–1577, 2017.
- [41] F. Milano and A. Ortega, "Frequency divider," *IEEE Trans. Power Syst.*, vol. 32, no. 2, pp. 1493–1501, 2017.
- [42] A. Crivellaro, A. Tayyebi, C. Gavriluta, D. Groß, A. Anta, F. Kupzog, and F. Dörfler, "Beyond low-inertia systems: Massive integration of grid-forming power converters in transmission grids," Submitted. Available at <https://arxiv.org/abs/1911.02870>.
- [43] "Final report - Queensland and south Australia system separation on 25 August 2018," AEMO, Tech. Rep., 2019.
- [44] G. Peponides, P. Kokotovic, and J. Chow, "Singular perturbations and time scales in nonlinear models of power systems," *IEEE Trans. Circuits Syst.*, vol. 29, no. 11, pp. 758–767, 1982.
- [45] L. Sigrist, I. Egido, and L. Rouco, "Principles of a centralized UFLS scheme for small isolated power systems," *IEEE Trans. Power Syst.*, vol. 28, no. 2, pp. 1779–1786, 2013.
- [46] T. Qoria, F. Gruson, F. Colas, X. Guillaud, M. Debry, and T. Prevost, "Tuning of cascaded controllers for robust grid-forming voltage source converter," in *Power Systems Computation Conference (PSCC)*, 2018.



Ali Tayyebi received his BSc degree in electrical engineering from the University of Tehran, Iran in 2012. In 2014 he received his MSc degree in engineering mathematics (joint MATHMODS program) from University of L'Aquila, and University of Hamburg in Italy and Germany respectively. In 2016, he received his second MSc degree in sustainable transportation and electric power systems (joint STEPS program) from La Sapienza, University of Nottingham and University of Oviedo respectively in Italy, UK and Spain. From 2014 to 2016, he was

the recipient of EU scholarship for master studies. In 2016, he joined Austrian Institute of Technology (AIT) in Vienna, Austria as a MSc thesis candidate and afterward joined AIT as research assistant. In 2017, he started his joint PhD project at AIT and Automatic Control Laboratory, Swiss Federal Institute of Technology (ETH) Zürich, Switzerland. His main research interest is the non-linear systems and control theory with applications to power system. In particular, his PhD research focuses on the design of grid-forming converter control for low-inertia power system.



Florian Dörfler (S'09–M'13) is an Associate Professor at the Automatic Control Laboratory at ETH Zürich. He received his Ph.D. degree in Mechanical Engineering from the University of California at Santa Barbara in 2013, and a Diplom degree in Engineering Cybernetics from the University of Stuttgart in 2008. From 2013 to 2014 he was an Assistant Professor at the University of California Los Angeles. His students were winners or finalists for Best Student Paper awards at the 2013/2019 European Control Conference, the 2016 American

Control Conference, and the 2017 PES PowerTech Conference. His articles received the 2010 ACC Student Best Paper Award, the 2011 O. Hugo Schuck Best Paper Award, the 2012–2014 Automatica Best Paper Award, and the 2016 IEEE Circuits and Systems Guillemin-Cauer Best Paper Award. He is a recipient of the 2009 Regents Special International Fellowship, the 2011 Peter J. Frenkel Foundation Fellowship, and the 2015 UCSB ME Best PhD award.



Dominic Groß (S'11 - M'15) is an Assistant Professor with the Department of Electrical and Computer Engineering Department at the University of Wisconsin-Madison, Madison, WI, USA. From 2016 to 2019 he was a postdoctoral researcher at the Automatic Control Laboratory of ETH Zürich, Switzerland and he was with Volkswagen Group's Research Division in Wolfsburg, Germany from 2014 to 2015. He received a Diploma degree in Mechatronics from the University of Kassel, Germany, in 2010, and a Ph.D. degree in Electrical Engineering from the

same university in 2014. His research interests include distributed control and optimization of complex networked systems with applications in power systems dominated by power electronic devices.



Adolfo Anta received the Licenciatura degree from ICAI Engineering School, Madrid, Spain, in 2002, and the M.Sc. and Ph.D. degrees from the University of California, Los Angeles, CA, USA, in 2007 and 2010, respectively. From 2002 to 2005, he was a Design Engineer with EADS-Astrium and, from 2010 to 2012, he was a Postdoctoral Researcher with the Technical University of Berlin and the Max Planck Institute, Germany. From 2012 to 2018 he worked as lead researcher at GE Global Research Europe, Germany. He is currently with Austrian

Institute of Technology AIT as research engineer in Vienna, Austria. His research interests cover a wide range of control applications, in particular stability issues in power systems. Dr. Anta received the Fulbright Scholarship in 2005, the Alexander von Humboldt Fellowship in 2011, was a Finalist for the Student Best Paper Award at the IEEE Conference on Decision and Control in 2008, and received the 2010 EMSOFT Best Paper Award and the IEEE CSS George S. Axelby Award in 2011.



Friederich Kupzog holds a Diploma degree in electrical engineering and information technology from RWTH Aachen, Germany. In 2006, he joined the Institute of Computer Technology at TU Wien, Austria, where he achieved his PhD Degree in 2008. Until 2012, he stayed at the university as a Post-Doc and built up the research group "Energy & IT" at the Institute of Computer Technology. Since 2012, Dr. Kupzog is Senior Scientist at the AIT Austrian Institute of Technology GmbH. His research interest lies in verification methods for networked Smart

Grid systems. He is the Head of Competence Unit Electrical Energy Systems since August 2018.